JOURNAL OF AIRCRAFT
Vol. 35, No. 1, January–February 1998

Numerical Analysis of the Interference Effect of Propeller Slipstream on Aircraft Flowfield

Qin E,* Guowei Yang,† and Fengwei Li‡
Northwestern Polytechnical University, Xi'an 710072, People's Republic of China

The panel method was used for the numerical calculations in this study. The propeller vortex system rotating with its blades, and the steady horseshoe vortex system distributed on the aircraft surface were used as the mathematical model. Neumann boundary conditions were satisfied at the panel control points of the blade and the aircraft panel to achieve coupling of propeller slipstream with the whole flowfield of the aircraft. At each corresponding azimuth angle of the propeller, pressure coefficients and induced velocities by the two vortex systems at the panel control points were calculated; from this, the average aerodynamic characteristics of the aircraft in one revolution period were obtained. The contraction effect of the three-dimensional propeller slipstream and its influence on the flowfield were considered in the computation. Results of numerical examples showed that the slipstream had a significant effect on aircraft lift characteristics such as flap deflecting, resulting in relatively large changes of the aircraft moment performance. Numerical results were in good agreement with the experimental data. The method presented here is suitable for both single- and multiple-propeller aircraft.

Nomenclature

C_D = drag coefficient of aircraft or wing
C_L = lift coefficient of aircraft or wing
C_M = moment coefficient of aircraft or wing
C_P = aircraft surface pressure coefficient
C_T = propeller thrust coefficient
D = influence coefficient matrix of aircraft vortex system
D_p = influence coefficient matrix of propeller vortex system
J = propeller advance ratio
N_b = number of blades
R = propeller radius
r = radial distance from propeller axis
α = geometric angle of attack
α_P = incidence of engine setting angle
$\{\Gamma_b\}$ = aircraft horseshoe vortex strength distribution
$\{\Gamma_p\}$ = propeller blade vortex strength distribution.
γ_i = dihedral angle of aircraft panel lattices
ΔC_L, ΔC_D, ΔC_M = aerodynamic characteristic increment of aircraft or wing
δ = flap deflection angle
ε_i = aircraft surface streamwise slopes at control points
θ = blade azimuth angle
ω = propeller rotational speed

I. Introduction

PROPELLER aircraft are still in use as passenger airplanes. To alleviate the problem of rising fuel costs, aircraft designers are developing advanced turboprop systems as practical propulsion alternatives. As a result, there have been efforts to understand and predict the mutual interference between propeller slipstream and aircraft flowfield. This has become an important focus in the area of computational fluid dynamics. Work was performed from the 1970s through the late 1980s[1–4] in this area. However, there are several shortcomings in applying the panel method to study propeller slipstream flowfield and the interference between the slipstream and the flowfield around the aircraft. For instance, the slipstream was modeled simply by concentric uniform vortex rings, and neither the effect of slipstream contraction nor the influence of the aircraft flowfield on propeller slipstream was taken into consideration. It is therefore necessary to improve the current methodology.

In this paper, the free wake analysis method was used in calculating the flowfield of an isolated propeller vortex wake and propeller performance parameters. The vortex lattice panel method was used in the flowfield around the power-off aircraft. Propeller slipstream–aircraft flowfield interference was simulated by the mutual interference between the helical trailing vortex system rotating with the propeller and the steady bound-horseshoe-vortex systems on the aircraft surface. Neumann boundary conditions were satisfied at the control points on both the aircraft surface panel and the propeller blade panel to achieve the coupling of the two vortex systems.

Using the numerical method presented in this paper, we calculated the aerodynamic characteristics of both the Chinese Y-7 aircraft with the propeller slipstream interference effect and the numerical example described in Ref. 3. The results were in good agreement with the experimental data.

II. Calculation of Isolated Propeller Slipstream Flowfield

The propeller blade constrained coordinate system was used and abbreviated as the propeller coordinate system (Fig. 1). This system coincided with the aircraft body axis system when the phase angle was zero.

The vortex lattice method lifting line theory was applied when the propeller blade aspect ratio was larger than six. For a propeller aspect ratio less than six, the lifting surface theory was used. The bound vortex was collocated at the quarter-chord line of every mesh, and the 3/4-mesh chord point was chosen as the control point. The strength of the bound vortex within the vortex lattice was constant, while the strength of the bound vortex between adjacent vortices jumped. At the two

---

Received March 26, 1997; revision received Aug. 18, 1997; accepted for publication Aug. 19, 1997.

*Associate Professor, Department of Aircraft Engineering, P.O. Box 114.

†Graduate Student, Department of Aircraft Engineering, P.O. Box 114.

‡Professor, Department of Aircraft Engineering, P.O. Box 114. Member AIAA.

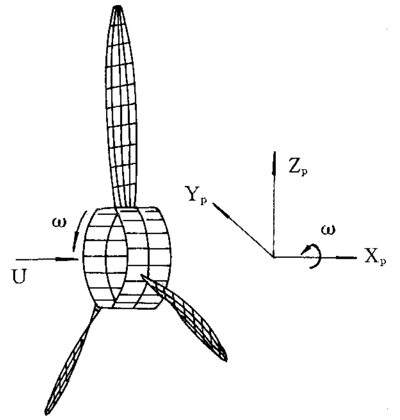

Fig. 1 Propeller coordinate system.

ends of each bound vortex, the trailing vortex is carried by the flow downstream, forming the equal-radius, equal-pitch, and half-infinite helical filaments. The strength of the half-infinite helical filament equals the difference of the adjacent bound vortices. The Goldstein helical trailing-vortex model was therefore constructed (Fig. 2).

The relative azimuth angles of other blades to the one along which the propeller coordinate system was constructed were as follows:

$$\theta_p = (2\pi/N_b)(k - 1) \qquad k = 1, 2, \ldots, N_b \tag{1}$$

The position of the helical vortex filament, which leaves downstream from the blade bound vortex at a distance ρ from the propeller axis, was determined by the following equation:

$$X = J\theta, \qquad Y = \rho \sin(\theta + \theta_p), \qquad Z = \rho \cos(\theta + \theta_p) \tag{2}$$

The induced velocity at any point by the vortex lattice bound vortex and its leaving helical trailing-vortex filament can be calculated using the Biot–Savart law.

The boundary condition of the flowfield on the body surface was satisfied at the control point. The resultant velocity at the control point was obtained by summarizing the freestream velocity, propeller rotational velocity, and was-induced velocity. When the boundary condition was applied to all the control points, we obtained a set of diagonal predominant algebraic equations with the vortex element strength as their variable. They could be solved by using the method of Gaussian elimination to obtain the circulation distribution.

The lift acting on the blade vortex element was calculated through the Kutta–Joukowski theory. When the profile drag was neglected, the lift was decomposed into components along the axial, radial, and tangential directions so that propeller characteristic parameters such as thrust, radial force, and tangential force could be evaluated.

To consider the propeller trailing-vortex wake contraction effect, the propeller trailing vortex was divided into a near-vortex wake region and a far-vortex wake region (Fig. 3). The near-wake region was composed of free-line vortex chain, and the trailing-vortex contraction effect was considered only in this region. The far-wake region consisted of the equal-pitch and equal-diameter helical vortex lines, determined by the last point parameter of the near-wake region. According to the experimental data and our experience, it is sufficient that the near-wake region extended to the first 450 deg downstream of the blade.

The iteration scheme of the free near wake was used as follows. Assume the velocity at the free vortex wake chain nodal point (r, θ, x) is

$$V = (V_r, V_\theta + \omega r, V_x + V_\infty)$$

where V_r, V_θ, and V_x are the three components of the nodal-point-induced velocity, respectively.

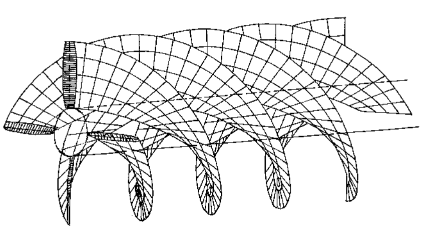

Fig. 2 Helical trailing-vortex model of Goldstein.

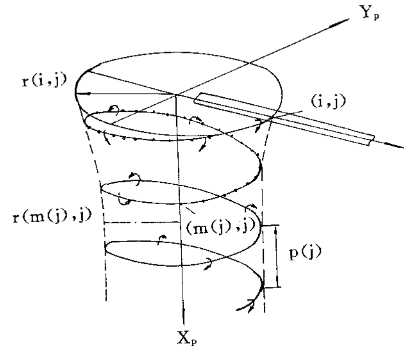

Fig. 3 Near- and far-vortex wake regions of the propeller trailing vortex.

Free proceeding was performed from one nodal point $(r, \theta,$ and $x)$ to the next $(r', \theta',$ and $x')$. The relationship of their coordinates can be described in the differential form

$$r' = r + \Delta r, \qquad \theta' = \theta + \Delta\theta, \qquad x' = x + \Delta x \tag{3}$$

where Δr, $\Delta\theta$, and Δx are the increments of the nodal coordinate. Their relationship with the nodal velocity is as follows:

$$\Delta r = [V_r/(V_\theta + \omega r)]r\Delta\theta, \qquad \Delta x = [(V_x + V_\infty)/(V_\theta + \omega r)]r\Delta\theta \tag{4}$$

where $\Delta\theta$ is an independent variable that represents the increase in azimuth angle of two adjacent vortex chain nodal points. Depending on the actual change of the propeller, the value of V_θ is small relative to ωr, and hence can be neglected. Substituting Eq. (4) into Eq. (3) and nondimensionalizing, we obtained the following:

$$\boldsymbol{r' = r + JV_r\Delta\theta, x' = x + J(1 + V_x)\Delta\theta} \tag{5}$$

This equation is the so-called free near-vortex wake contraction iteration scheme.

To make the computation stable and accelerate the convergence rate of iteration, the preceding scheme was then changed into the relaxation iteration scheme:

$$\begin{aligned} \boldsymbol{r}'^{\mathrm{NEW}} &= (1 - \varepsilon_r)\boldsymbol{r}'^{\mathrm{OLD}} + \varepsilon_r(\boldsymbol{r} + JV_r\Delta\theta) \\ \boldsymbol{x}'^{\mathrm{NEW}} &= (1 - \varepsilon_x)\boldsymbol{x}'^{\mathrm{OLD}} + \varepsilon_x[\boldsymbol{x} + J(1 + V_x)\Delta\theta] \end{aligned} \tag{6}$$

where ε_r and ε_x are the radial and axial displacement relaxation factors, respectively. The superscript OLD represents the preceding iteration value, and NEW represents the current value. The trailing-vortex wake model of contraction was obtained through successive iteration.

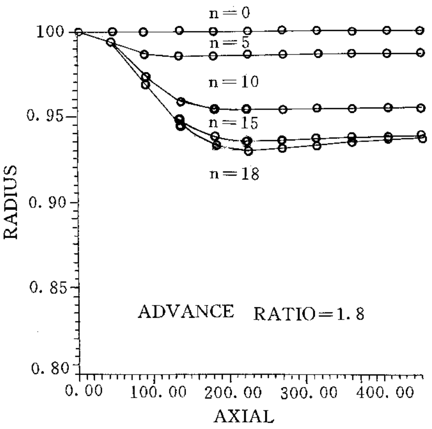

Fig. 4 Radial locations of the tip vortex at various iterations.

Figure 4 shows the changes of the propeller wake contraction radius corresponding to the number of iterations for the Y-7 aircraft. It is clear that the propeller near-wake contraction value can reach 10%. The value of ε_r and ε_x was chosen as 0.5 during computation.

III. Calculation of Aerodynamic Forces (Power-Off)

The horseshoe vortex was collocated at the quarter-chord line of the aircraft surface lattice, and the 3/4-chord point of the lattice was chosen as the control point. The boundary value problem of the flow on the lifting surface could be transformed into the problem of an integral equation that connected the normal wash with the loading distribution. Therefore, the downwash-induced velocity at the ith lattice control point by the jth lattice vortex was

$$W_{A_{ij}} = \frac{C_{pi}}{8\pi} \Delta X_j \int_{-l_j}^{l_j} K(X - \xi, Y - \eta, Z - \zeta, M_\infty)\, d\sigma$$

i.e.,

$$W_A = DC_p \tag{7}$$

Using the Biot–Savart law we could calculate the induced velocity at any spatial point caused by the horseshoe vortex with vortex strength Γ. For the aircraft body coordinates, we obtained

$$\{U\} = P\Gamma, \qquad \{V\} = Q\Gamma, \qquad \{W\} = R\Gamma \tag{8}$$

where $\Gamma = V_\infty[\Delta X_j/2]C_p$. The normal induced velocity should be aligned in the normal direction of the wing surface, hence

$$D = [\cos \gamma_j]R[\Delta X_j/2] + [\sin \gamma_j]Q[\Delta X_j/2] \tag{9}$$

where γ_j is the dihedral angle on the jth panel. The normal wash W_A could be determined by the body surface slope at the control point according to the body surface tangency condition. Once D was solved, C_P could be determined.

IV. Calculation of Interference Between Propeller Slipstream and Flowfield Around Aircraft

A. Interference Model

The interference between the slipstream and the flowfield around the aircraft could be simulated by the interference between the helical vortex system and the aircraft vortex system. Once the instantaneous relative positions of the two vortex systems were determined, the instantaneous interference between the two vortex systems could be calculated using the Biot–Savart law. Therefore, in consideration of the slipstream influence, we calculated the instantaneous value of the aircraft aerodynamic characteristics corresponding to changes of the propeller phase angle, as well as the average value of the aircraft aerodynamic characteristics in one rotational period.

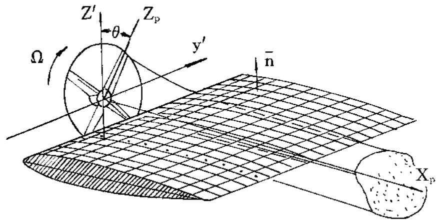

Fig. 5 Relative spatial position of the propeller coordinate system to the aircraft body coordinate system.

B. Interference Effect of Propeller Slipstream on Flowfield Around Aircraft

The computation of the propeller's interference effect on the aircraft should be performed using the propeller coordinate system. The relative spatial position of the propeller coordinate system to the aircraft body frame coordinate system is shown in Fig. 5. Assuming that a spatial point Q_i in the aircraft body coodinate system is (X_{bi}, Y_{bi}, Z_{bi}), its transformation into the propeller coordinate system is given by

$$\begin{aligned} X_{pi} &= \Delta X_i \cos \alpha_p - \Delta Z_i \sin \alpha_p \\ Y_{pi} &= \Delta Y_i \cos \theta - [\Delta Z_i \cos \alpha_p + \Delta X_i \sin \alpha_p]\sin \theta \\ Z_{pi} &= [\Delta Z_i \cos \alpha_p + \Delta X_i \sin \alpha_p]\cos \theta + \Delta Y, \sin \theta \end{aligned} \tag{10}$$

where $\Delta X_i = (X_{bi} - X_{p0})$, $\Delta Y_i = (Y_{bi} - Y_{p0})$, and $\Delta Z_i = (Z_{bi} - Z_{p0})$. X_{p0}, Y_{p0}, and Z_{p0} are the coordinates of the origin point of the propeller coordinate system in the aircraft body system.

From Eq. (10), the coordinates of the aircraft surface panel control point for a given azimuth angle in the propeller coordinate system could be determined. By computing the propeller vortex wake flowfield, the influence coefficient and the induced velocity $U'_{pi}(\theta, \alpha_p)$, $V'_{pi}(\theta, \alpha_p)$, $W'_{pi}(\theta, \alpha_p)$ at the aircraft surface panel control points caused by the propeller vortex system could be solved. Transforming back to the aircraft body frame coordinate system, we obtained

$$\begin{aligned} U_{pi} &= U'_{pi} \cos \alpha_p + (W'_{pi} \cos \theta - V'_{pi} \sin \theta)\sin \alpha_p \\ V_{pi} &= V'_{pi} \cos \theta + W'_{pi} \sin \theta \\ W_{pi} &= (W'_{pi} \cos \theta - V'_{pi} \sin \theta)\cos \alpha_p - U'_{pi} \sin \alpha_p \end{aligned} \tag{11}$$

The normal induced velocity at the control points of the aircraft surface panel was

$$W_{NPi}(\theta, \alpha_p) = (W_{pi} \cos \gamma_i - V_{pi} \sin \gamma_i)\cos \varepsilon_i - U_{pi} \sin \varepsilon_i$$

When the slipstream interference effect is considered, the sum of the normal downwash at the aircraft panel control point should be the resultant downwash induced by both the power-off aircraft vortex system and the propeller vortex system. At the body surface boundary points, $W_N \cdot n = 0$, i.e.,

$$\{W_B\} + \{W_{\mathrm{NP}}\} + \{W_\infty\} = 0 \tag{12}$$

where $\{W_B\} = [D]\{C_p\}$, $\{W_{\mathrm{NP}}\}$ is the normal induced velocity by the propeller vortex system, and $\{W_\infty\}$ is defined by the freestream and the body boundary slope. Substituting into Eq. (12)

$$[D]\{C_p\} = -\{W_\infty\} - \{W_{\mathrm{NP}}\} \tag{13}$$

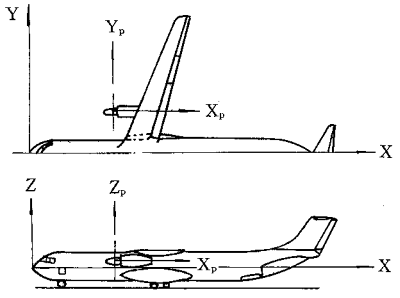

Fig. 6 Body frame coordinate system.

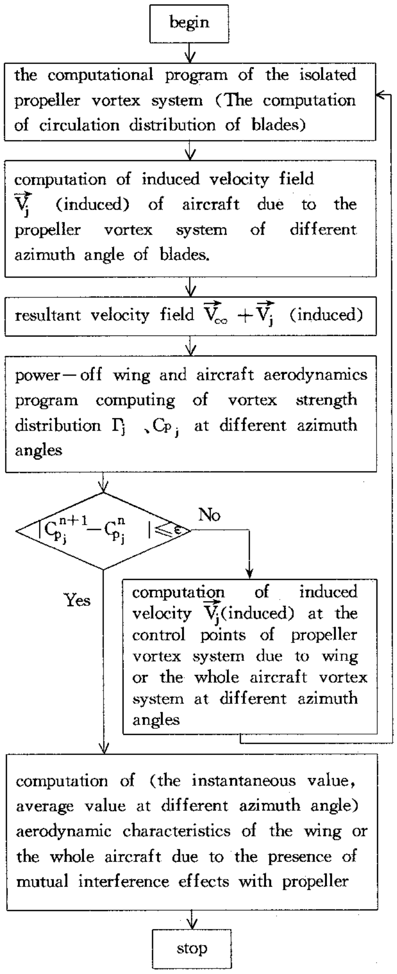

Fig. 7 Computational program flowchart of propeller slipstream and whole aircraft interference.

The relation $C_p = C_p(\theta, \alpha_p, C_T)$ holds at the aircraft surface panel control points.

C. Aircraft Interference Effect on Propeller Slipstream

The computation should be performed in the body frame coordinate system (Fig. 6). In the same way, the coordinates of the propeller blade panel control points should be transformed into the body frame coordinate system. $U'_{bi}(\alpha, \theta)$, $V'_{bi}(\alpha, \theta)$, $W'_{bi}(\alpha, \theta)$ at the propeller blade panel control points by the aircraft vortex system can be obtained by utilizing the code for the power-off aircraft. Transforming back to the propeller coordinate system, we obtained the corresponding normal induced velocity $W_{Nbi} = W_{bi} \cdot N_{pi}$, where N_{pi} is the normal direction of the propeller blade panel control point. At the propeller blade panel control point, we have

$$\{W_{NPS}\} + \{W_{Nb}\} + \{W_N\} = 0 \tag{14}$$

where $\{W_N\} = [D_p]\{\Gamma\}$, $[D_p]$ is the normal aerodynamic influence coefficient of the propeller vortex system, and $\{W_{NPS}\}$ is the normal component at the propeller blade control point of the freestream and the propeller rotation velocity. It is clear that $\{\Gamma\}$ caused by the interference effect of the aircraft vortex system can be determined.

D. Effect of Slipstream Momentum on Aerodynamic Characteristics

The momentum increase of the aircraft flowfield caused by the slipstream can also influence the aircraft's aerodynamic characteristics. In this paper, the propeller vortex system-induced streamwise velocity at the panel control point was calculated. The velocity was then added to the uniform freestream

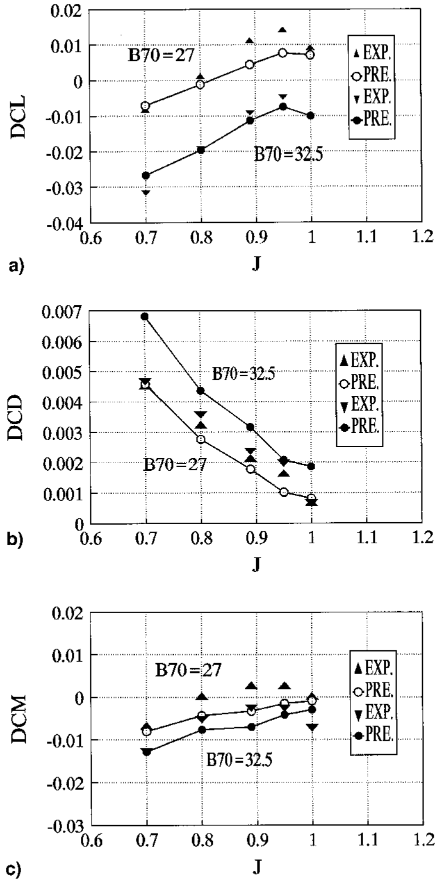

Fig. 8 Slipstream influence effect on the aerodynamic characteristics a) ΔC_L, b) ΔC_D, and c) $\Delta C_M$of the wing.

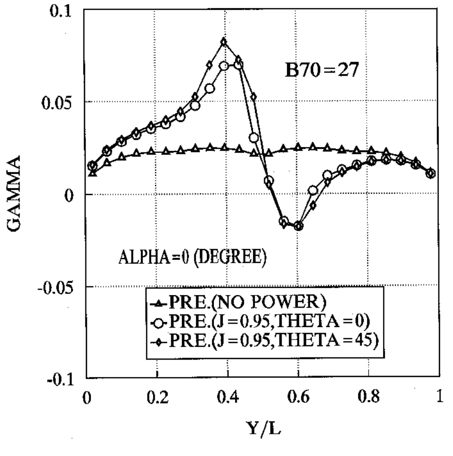

Fig. 9 Wing circulation spanwise distribution.

velocity field to determine the effect of the flowfield momentum increase.

V. Coupling the Interference Between Propeller Slipstream and Flowfield Around Aircraft

The solution to the isolated propeller and flowfield around a power-off aircraft and the corresponding Γ^0 and C_P^0 can be obtained from their respective preceding sections. For the propeller circulation, Γ^0, its interference on the whole aircraft and corresponding C_P' can be calculated from Sec. IV.B. Conversely, for C_P^0, its interference on the propeller and the corresponding Γ' can be calculated from Sec. IV.C. Such repeated iterations were performed until $\Gamma^{n+1} - \Gamma^n$ and $C_P^{n+1} - C_P^n$ reached the required precision. In general, five iterations were required for a converged solution, when $|C_P^{n+1} - C_P^n|/C_{Pj}^n \leq 10^{-2}$. Figure 7 shows a flowchart of the coupled iteration procedure.

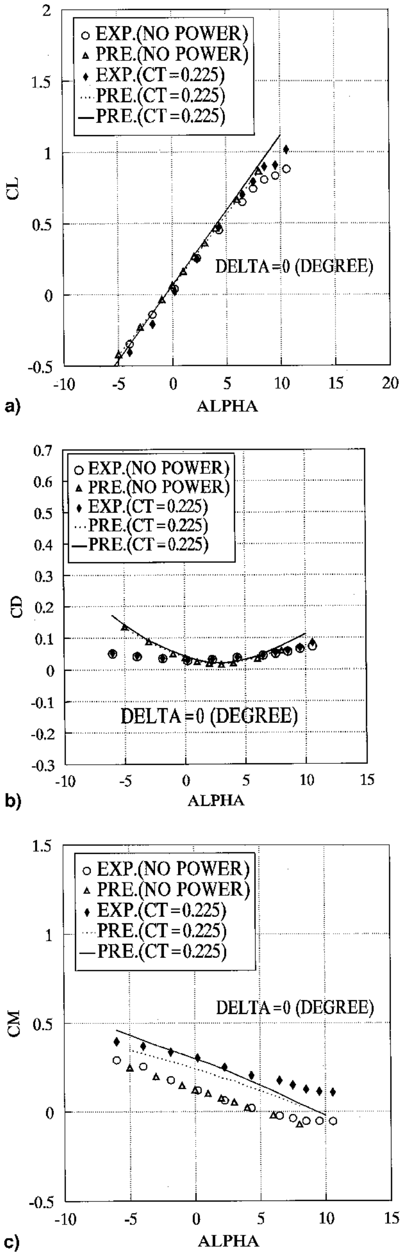

Fig. 10 a) C_L, b) C_D, and c) C_M as a function of α at $\delta = 0$ deg for the Y-7 transport aircraft. The dotted curve represents the effective angle of attack variation caused by slipstream effects. The solid line represents the effective angle of attack variation and momentum variation caused by slipstream effects.

VI. Numerical Results and Discussion

In this paper, we calculated the aerodynamic characteristics of the wing–nacelle–slipstream interference model[3] and the Chinese Y-7 passenger airplane at various flap deflections and thrust coefficients. Some typical results follow.

Figure 8 shows the computation of the wing ΔC_L, ΔC_D, and ΔC_M induced by the slipstream at different pitch angles and different advanced ratios in the model,[3] and their comparison with the experimental data.[3] In Fig. 8, B70 represents the pitch angle at 0.7 spanwise length of the blade.

Figure 9 shows the computation of the wing circulation spanwise distribution by the power-off wing and the slipstream at different θ (degree) of propeller in the model.[3]

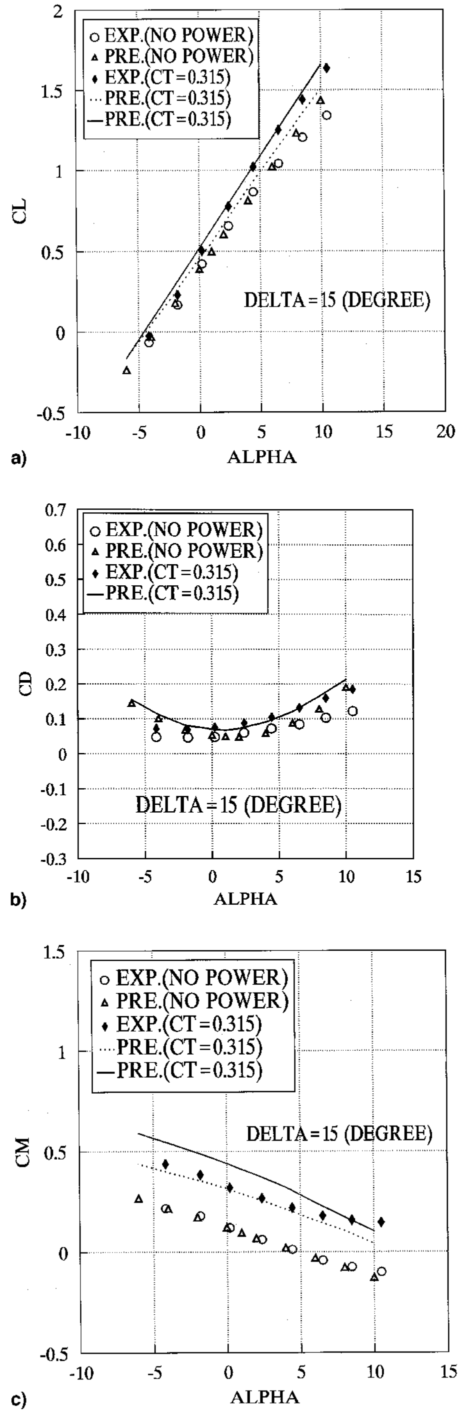

Fig. 11 a) C_L, b) C_D, and c) C_M as a function of α at $\delta = 15$ deg for the Y-7 aircraft.

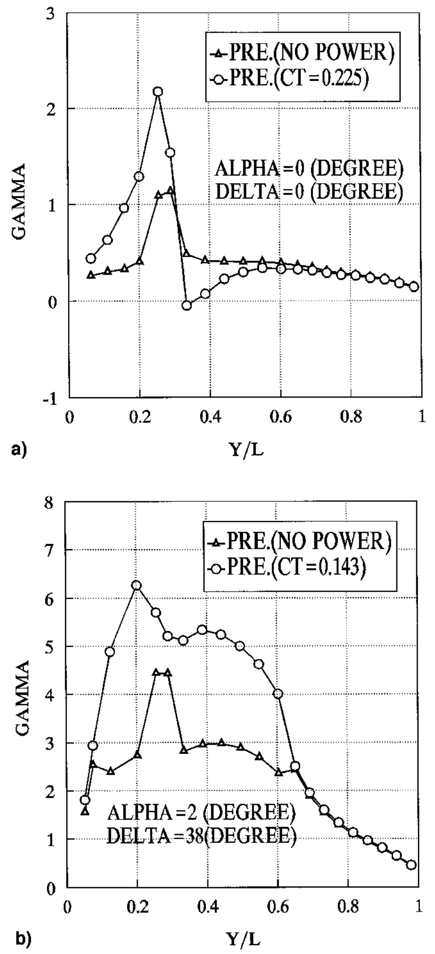

Fig. 12 Wing circulation spanwise distribution of the Y-7 aircraft.

Figures 10 and 11 show the computed C_L, C_D, and C_M vs α curve and its comparison with the experimental data for the Y-7 at δ = 0 deg, C_T = 0.225 and δ = 15 deg, C_T = 0.315, respectively. Figure 12 shows the variations of the spanwise circulation distribution of the Y-7 wing at δ = 0 deg, C_T = 0.225 and δ = 38 deg, C_T = 0.143.

The following can be seen from these results: In the cruising region (δ = 0 deg), the slipstream had very little influence on the whole aircraft lift. The lift increase was only about 5% (Fig. 10a). As the flap was deflected, the influence of slipstream caused a significant increase in the aircraft lift. The numerical results are in good agreement with the experimental data (Fig. 11a). As the flap was deflected, slipstream influence also caused the wing lift to be increased at both the inner and outer sides of the nacelle. However, without flap deflection, only the lift of the inner-side wing had increases, whereas the lift of the outer-side wing decreased (Fig. 12). These conclusions are consistent with other reports on similar types of aircraft[4–7] in the lift range considered.

Viscous drag is neglected in this paper. The slipstream caused a small increase in induced drag when the flap was not deflected. As the flap deflection angle and thrust coefficient increased, the range of drag increase was significant. The calculated value of the drag increase is in good agreement with the experimental data.

The influence of the propeller slipstream on the aircraft's pitching moment is rather complicated. The horizontal tail is immersed in the wing wake and the field of slipstream at the same time. The aerodynamic load of the horizontal tail depends not only on the relative position of the wing, but also on the relative position of the propeller and the change of its angle of attack and thrust coefficient. As shown in Figs. 10c and 11c, the numerical results are in agreement with the experimental data in the region of a small angle of attack. As the angle of attack increased, the discrepancy increased. The discrepancy became severe when the flap deflection and thrust coefficient increased. The reason could be that the simulation of the spatial position of the propeller trailing-vortex wake in the region of a large angle of attack was not accurate, and the viscous effects were not considered.

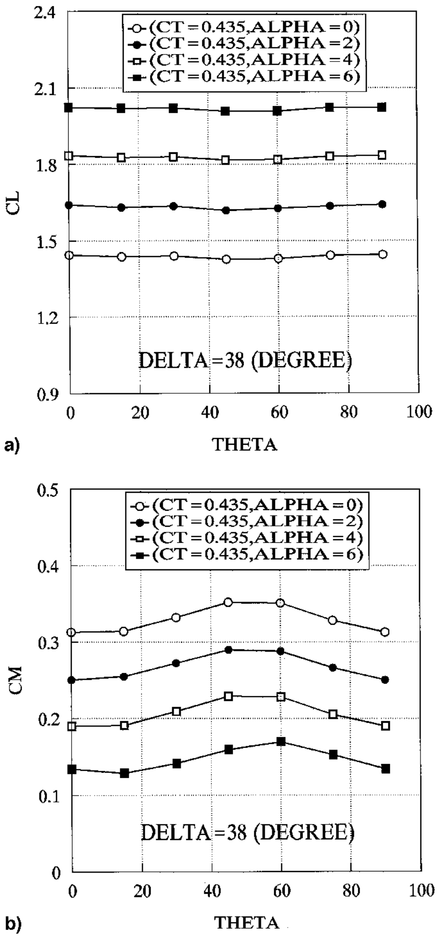

Fig. 13 a) C_L and b) C_M as a function of θ at δ = 38 deg for the Y-7 aircraft.

To demonstrate the unsteady effect of slipstream interference, variations of C_L and C_M vs θ during one period at C_T = 0.435 in the Y-7 aircraft are shown in Fig. 13. The period is determined by the number of propeller blades.

VII. Conclusions

In this paper, the lift surface vortex lattice method was used to compute propeller slipstream, which is under vortex wake contraction conditions, and power-off aircraft surface pressure distribution and aerodynamic characteristics. Based on this, computation of the coupling between the slipstream flowfield and the whole aircraft flowfield was achieved. The whole aircraft's aerodynamic characteristics corresponding to each propeller azimuth angle were solved, as was the average of the whole aircraft's aerodynamic characteristics in one revolution period. Both the interference of propeller slipstream on the whole aircraft's aerodynamic characteristics and that of the aircraft on the slipstream flowfield were considered in the coupling method.

As shown by the results of the two numerical examples, each with a large amount of experimental data, the slipstream–whole aircraft coupling computation method applied in this paper is correct. The numerical results of the aircraft lift characteristics and the drag characteristics are in good agreement with the experimental data; however, there is some deviation between the calculated pitching moment characteristics and the experimental data. It is believed that, because the influence of propeller slipstream on the pitching moment of the whole aircraft depends mainly on the slipstream's interference on the flowfield around the horizontal tail, both the numerical simulation and the experimental study require further investigation.

References

[1] Frecman, C. E., "Development and Validation of a Combined Rotor–Fuselage Induced Flow-Field Computational Method," NASA TP 1656, June 1980.

[2] Chandrasekaran, B., "Method for Calculating Effects of a Propfan on Aircraft Aerodynamics at Subsonic Speed," AIAA Paper 83-1216, June 1983.

[3] Favier, D., Ettaouil, A., Maresca, C., and Barbi, C., "Experimental and Numerical Study of Propeller Wakes in Axial Flight Regime," International Council of the Aeronautical Sciences, 88-2.4.4, Sept. 1988, pp. 602–616.

[4] Aljabri, A. S., "Aerodynamic Design of Propfan Powered Transports," AIAA Paper 83-1213, June 1983.

[5] Yang, G.-W., and He, Z.-D., "Computation of Propeller Slipstream on Account of the Contraction Effect of the Trailing Vortex Wake," *Acta Aerodynamica Sinica*, Vol. 13, No. 6, 1995, pp. 83–86.

[6] Boctor, M. L., Clay, C. W., and Watson, C. F., "An Analysis of Prop-Fan/Airframe Aerodynamic Integration," NASA CR-152186, Oct. 1978.

[7] Fratell, G., Favier, D., and Maresca, C., "Experimental and Numerical Study of the Propeller/Fixed Wing Interaction," *Journal of Aircraft*, Vol. 28, No. 6, 1991, pp. 365–373.